Expert Systems With Applications 288 (2025) 128277

Contents lists available at ScienceDirect

Expert Systems With Applications

journal homepage: www.elsevier.com/locate/eswa

Correction of non-anechoic antenna measurements using matrix pencil algorithm with adaptively adjusted setup

Adrian Bekasiewicz

Faculty of Electronics, Telecommunications and Informatics, Gdansk University of Technology, Narutowicza 11/12, 80-233 Gdansk, Poland

ARTICLE INFO

Keywords:
Adaptive correction setup
Antenna measurements
Compact antennas
Matrix-pencil algorithm
Non-anechoic experiments
Radiation pattern measurements

ABSTRACT

Far-field antenna performance is normally evaluated in dedicated test sites such as anechoic chambers. Although capable of providing certification-grade accuracy, professional laboratories are prohibitively expensive. Alternatively, measurements can be performed in non-anechoic conditions and then refined using appropriate algorithms. Unfortunately, post-processing performance depends on the routine-specific setup, which is either determined based on engineering insight or rules-of-thumb. In this work, a refinement of far-field experiments performed in uncontrolled environments, with a focus on automatic tuning of the correction setup has been proposed. The method involves optimization of the post-processing algorithm (here, a matrix-pencil method) setup so as to minimize the discrepancy between the refined responses and an iteratively updated surrogate obtained through non-linear tuning of uniformly scaled EM simulations. The method has been validated based on measurements of two planar antennas at two test sites at 15 unique frequencies. The tests include a performance benchmark against the correction with a manual setup, but also comparisons against the state-of-the-art algorithms, and stochastic optimization approaches. Overall, a total of 400 experiments have been performed. For the considered correction algorithm and antennas, the proposed method offers over 14 dB higher fidelity of the refined responses compared to manual setups.

1. Introduction

Evaluation of far-field performance is a crucial step in the development of new antenna structures. The task is normally performed in professional laboratories such as anechoic chambers (ACs), or compact-range test sites that ensure strict control over the propagation environment (Hemming, 2002; Parini et al., 2020). Although the mentioned facilities can ensure certification-grade accuracy, their construction is prohibitively expensive. Furthermore, the high cost might not be justified for applications where the fidelity of measurements is not of utmost concern, i.e., for teaching, research, or rapid iteration of prototype structures. For the first scenario, the procedures associated with the evaluation of specific performance figures are more important than the accuracy of the obtained results. Furthermore, the use of cheap test gear reduces expenses in the event of mishandling by personnel in training. When research, or rapid development are considered, the prototypes are not intended for mass production. Instead, the main goal of experiments is to evaluate the quality of electromagnetic (EM) models used for their development. Certain discrepancies between simulation and measurement results are considered acceptable, as they often stem from the model simplifications such as relaxed discretization and/or neglected components of the antenna (e.g., housing or connectors) (Esmail et al., 2024; Lyu et al., 2023; Rice & Kiourti, 2022; Wu et al., 2023). For the considered examples, measurements in non-anechoic environment represent an interesting—and cost-efficient—alternative to evaluation of antenna performance in professional facilities. On the other hand, the noise and interference resulting from multi-path propagation render the far-field responses obtained in uncontrolled conditions of little to no use for drawing meaningful conclusions about the performance of the antenna under test (AUT) (Awan & Kiran, 2017; Gbadamosi et al., 2024; Ghosh et al., 2024).

The problem concerning inaccuracy of measurements performed in non-anechoic environments can be mitigated using appropriate post-processing methods. The available algorithms fall into two main categories: (i) multi-frequency experiments and (ii) extraction of test-environment imperfections (Araque Quijano et al., 2011; Bekasiewicz et al., 2023; Cano-Facila et al., 2011; de Sao Jose et al., 2020; Fourestie & Altman, 2001; Froes et al., 2019; Gemmer & Heberling, 2020; Gregson et al., 2011; Loredo et al., 2004; Sarkar & Pereira, 1995; Soltane et al., 2020). Frequency-based approaches involve evaluation of responses

E-mail address: adrian.bekasiewicz@pg.edu.pl.

https://doi.org/10.1016/j.eswa.2025.128277
Received 20 December 2024; Received in revised form 11 May 2025; Accepted 20 May 2025
Available online 22 May 2025

between the reference antenna (RA) and the AUT as a function of the AUT angular position over a bandwidth of interest so as to identify signal components pertinent to the line-of-sight (LoS) transmission. The useful part of the signal can be extracted based on analysis in the time domain, followed by modification of the response using carefully selected kernels (Bekasiewicz et al., 2023; Loredo et al., 2004), or through reconstruction of the frequency responses from a composition of appropriate basis functions (Fourestie & Altman, 2001; Sarkar & Pereira, 1995). The second class of methods involves multiple measurements at pre-determined locations around the AUT so as to extract data on properties of the propagation environment. The available approaches include spatial filtering of reflected signals (Cano-Facila et al., 2011), determination of the test zone field based on evaluation of responses (Gemmer & Heberling, 2020), mode orthogonalization through experiments with a displaced RA (Gregson et al., 2011), or extraction of equivalent currents on the hull enclosing the AUT (Araque Quijano et al., 2011). The main advantage of multi-test methods boils down to their applicability in the single-frequency regime. At the same time, spectrum-based approaches limit the useful range of measurement gear due to the need to acquire the AUT response over a bandwidth around the frequency of interest. On the other hand, the need to perform a range of repetitive experiments poses a significant challenge for less experienced engineers. In contrast, the configuration of multi-frequency experiments is similar to that required for AC-based tests, making them straightforward to use even for *en masse* measurements. Furthermore, the usefulness of these methods has been demonstrated in challenging conditions that include applications in non-anechoic environments, as well as the evaluation of small low-gain antennas, whereas test-environment extraction methods are often demonstrated in idealized conditions (e.g., ACs with installed reflective surfaces) and/or using relatively large, high-gain radiators (Cano-Facila et al., 2011; Fourestie & Altman, 2001; Loredo et al., 2004).

Regardless of the demonstrated usefulness, the performance of multi-frequency techniques heavily relies on the setup of the algorithm-specific hyperparameters (Bekasiewicz et al., 2023). The available literature lacks rigorous methodologies for estimating the settings applicable to post-processing of the measurements at hand. Instead, the guidelines concerning, e.g., the determination of appropriate bandwidth, frequency step, specific kernels and their intervals, or other parameters, are provided (Bekasiewicz et al., 2023; de Sao Jose et al., 2020; Fourestie & Altman, 2001; Sarkar & Pereira, 1995; Soltane et al., 2020). Recent findings indicate that the mentioned parameters are not only unique to the given temporal and spatial configuration of the test site but also vary as a function of operational frequency (Bekasiewicz & Waladi, 2024). Consequently, the post-processing setup should be determined based on a thorough, systematic analysis of propagation conditions rather than rule-of-thumb approaches. The problem here is that the existing methods do not embed the mechanisms dedicated to estimating quality of correction. The fidelity of the refined responses obtained in non-anechoic conditions is normally scrutinized through their comparison with the responses obtained in professional facilities. Although acceptable during method development (or validation), the lack of feedback on correction performance coupled with reliance on manual (or semi-manual) setup challenges the concept of post-processing for practical experiments in non-anechoic environments. The problem seems especially important when the fidelity of corrected responses is low. Determining whether the discrepancies between the simulations and measurements are due to poor correction performance or simplifications introduced to the EM simulation model can be challenging. From this perspective, the problem of automatic and reliable multi-frequency post-processing of far-field measurements in uncontrolled conditions remains open.

In this work, an algorithm for automatic determination of the correction setup for multi-frequency post-processing of non-anechoic measurements has been proposed. The method is implemented as a curve-fitting process where the input parameters of the correction routine are adjusted so as to match the refined non-anechoic antenna response to an iteratively updated surrogate, which is obtained through automatic non-linear tuning (angle-wise) and uniform scaling of the EM simulated radiation pattern. The proposed mechanism has been integrated with a matrix-pencil algorithm (MPA). The latter is capable of ensuring a high correction performance, provided that the appropriate setup of parameters has been determined (Bekasiewicz & Waladi, 2024; Loredo et al., 2004). The framework has been demonstrated using the measurements of two planar antennas at two non-anechoic test sites. A benchmark of post-processing performance against the MPA with the rule-of-thumb-based setups and alternative correction algorithms has also been provided. The new contributions of the work include: (i) the development of a deterministic, surrogate-based framework for automatic adjustment of the post-processing algorithm hyperparameters, (ii) thorough validation of the method across a set of experiments spanning 15 frequencies, and (iii) a detailed comparison of the approach against the state-of-the-art algorithms from the literature. The main innovation behind the proposed framework involves the use of optimization methods to achieve gradual bi-directional matching between the appropriately scaled EM-simulation model responses and the corrected non-anechoic measurements to alleviate the effects of magnitude misalignment and/or shifts in radiation nulls on post-processing performance. Overall, a total of 400 experiments have been performed. The presented mechanism can be used to obtain high-fidelity measurements in challenging propagation conditions without user interference.

2. Correction methodology

Post-processing of non-anechoic measurements involves manipulation of the RA-AUT system responses. This section provides the formulation of the problem along with a generic outline of the correction process. To ensure self-consistency, a brief discussion of the matrix-pencil routine used for response refinement is also included. The surrogate-assisted methodology for automatic adjustment of algorithm setup is discussed in Section 3.

2.1. Problem formulation

Let $\boldsymbol{R}_u(\boldsymbol{\omega}, \boldsymbol{\theta}, \boldsymbol{\varphi}, \boldsymbol{\rho})$ denote a complex matrix of uncorrected transmission S_{21} responses obtained between the RA and the AUT in the non-anechoic test environment, where $\boldsymbol{\omega} = [\omega_1 \ldots \omega_k]^T$ $(k = 1, \ldots, K)$ represents a sweep around the frequency of interest $f_0 = (\omega_K - \omega_1)/2$, with a step of $\delta\omega = \omega_k - \omega_{k-1}$ and a bandwidth around f_0 of $B = \omega_K - \omega_1$, whereas $\boldsymbol{\theta} = [\theta_1 \ldots \theta_A]^T$, $\boldsymbol{\varphi} = [\varphi_1 \ldots \varphi_B]^T$ are the spherical coordinates of the AUT w.r.t. RA; $\boldsymbol{\rho} = [\rho_1 \ldots \rho_C]^T$ represents a polarization-related rotation of the antenna system (note that A, B, and C are cardinalities of $\boldsymbol{\theta}$, $\boldsymbol{\varphi}$, and $\boldsymbol{\rho}$, respectively). In this work, data is acquired only in the elevation plane (hence, $\varphi = \pi/2$) while the RA rotation is set to $\rho = \pi/2$ (Bekasiewicz et al., 2023; Gemmer & Heberling, 2020). From this perspective, and for simplicity of notation, the transmission can be represented as a $K \times A$ matrix $\boldsymbol{R}_u = \boldsymbol{R}_u(\boldsymbol{\omega}, \boldsymbol{\theta}) = \boldsymbol{R}_u(\boldsymbol{\omega}, \boldsymbol{\theta}, \pi/2, \pi/2)$ where:

$$\boldsymbol{R}_u(\boldsymbol{\omega}, \boldsymbol{\theta}) = \begin{bmatrix} R_u(\omega_1, \theta_1) & \cdots & R_u(\omega_1, \theta_A) \\ \vdots & \ddots & \vdots \\ R_u(\omega_K, \theta_1) & \cdots & R_u(\omega_K, \theta_A) \end{bmatrix} \tag{1}$$

The goal of post-processing is to obtain the $\boldsymbol{R}_c(f_0, \boldsymbol{\theta})$ response which represents an approximation of the measurements performed at a professional test site (e.g., AC). For multi-frequency experiments, the correction is performed using the following generic framework:

1. Measure $\boldsymbol{R}_s(\boldsymbol{\omega}, \boldsymbol{\theta})$ in uncontrolled environment, set $a = 1$;
2. Obtain $\boldsymbol{R}_c(\boldsymbol{\omega}, \theta_a)$ from $\boldsymbol{R}_s(\boldsymbol{\omega}, \theta_a)$ using a suitable algorithm;
3. If $a < A$, set $a = a + 1$ and go to Step 2; otherwise extract $\boldsymbol{R}_c(f_0, \boldsymbol{\theta})$ from $\boldsymbol{R}_c(\boldsymbol{\omega}, \boldsymbol{\theta})$ and END.

For one-shot experiments (here, understood as non-anechoic measurements performed once over the selected bandwidth per each RA-AUT angle $a = 1, \ldots, A$), the post-processing in Step 2 can be realized in time- or frequency-domain. Here, the process is conducted using the matrix-pencil method outlined below.

2.2. Matrix-pencil algorithm

The algorithm approximates a complex RA-AUT transmission $\boldsymbol{R}(\boldsymbol{\omega}) = \boldsymbol{R}(\boldsymbol{\omega}, \theta_a)$:

$$\boldsymbol{R}(\boldsymbol{\omega}) = \sum_{m=1}^{M} r_m z_m^{\kappa} \tag{2}$$

where $\boldsymbol{z} = [z_1 \ldots z_m]^T$ and $\boldsymbol{r} = [r_1 \ldots r_m]^T$ ($m = 1, \ldots, M$) represent exponential functions and residues; $\boldsymbol{\kappa} = [0 \ldots K-1]^T$. Let $\boldsymbol{H} = \boldsymbol{H}(\boldsymbol{\omega}) = \boldsymbol{U}(\boldsymbol{\omega})\boldsymbol{\Sigma}(\boldsymbol{\omega})\boldsymbol{V}(\boldsymbol{\omega})^*$, where $\boldsymbol{U}$, $\boldsymbol{V}$ comprise eigenvectors and $\boldsymbol{\Sigma}$ is a diagonal matrix of singular values of $\boldsymbol{H}$ (the symbol "*" is a Hermitian transpose). The Hankel matrix is of the form (Sarkar & Pereira, 1995):

$$\boldsymbol{H}(\boldsymbol{\omega}) = \begin{bmatrix} R_u(\omega_1) & R_u(\omega_2) & \cdots & R_u(\omega_L) \\ R_u(\omega_2) & R_u(\omega_3) & \cdots & R_u(\omega_{L+1}) \\ \vdots & \vdots & \ddots & \vdots \\ R_u(\omega_{K-L-1}) & R_u(\omega_{K-L}) & \cdots & R_u(\omega_{K-1}) \end{bmatrix} \tag{3}$$

where $L \in [M; K-M]$ is a so-called pencil parameter. The components of $\boldsymbol{z}$ are eigenvalues of $\boldsymbol{Y}_1^{+}\boldsymbol{Y}_2$ (where "+" denotes a pseudo-inverse). The respective matrices are $\boldsymbol{Y}_1 = \boldsymbol{U}\boldsymbol{\Sigma}_M\boldsymbol{V}_1^*$ and $\boldsymbol{Y}_2 = \boldsymbol{U}\boldsymbol{\Sigma}_M\boldsymbol{V}_2^*$, where $\boldsymbol{\Sigma}_M$ comprises only the first M columns of $\boldsymbol{\Sigma}$; $\boldsymbol{V}_1$ and $\boldsymbol{V}_2$ consist of all but the first and all but the last row of $\boldsymbol{V}_M$, respectively; $\boldsymbol{V}_M$ contains all rows and the first M columns of $\boldsymbol{V}$. The vector of residues is obtained by solving the least-squares problem $\boldsymbol{r} = \boldsymbol{Z}^{+}\boldsymbol{R}(\boldsymbol{\omega})$, where $\boldsymbol{Z}$ is a Vandermonde matrix constructed from $\boldsymbol{z}$ (Sarkar & Pereira, 1995).

It should be noted that the MPA automatically identifies $\boldsymbol{z}$ and $\boldsymbol{r}$ components pertinent to the LoS transmission between the RA-AUT system components. Let $\boldsymbol{t}_a = [t_{a.1} \ldots t_{a.m}]^T$ be the vector of LoS delays with mth component given as:

$$t_{a.m} = \tan^{-1}\left(\frac{\Im(z_m)}{\Re(z_m)}\right)(\delta\omega \cdot 2\pi)^{-1} \tag{4}$$

The corrected response is of the form $\boldsymbol{R}_c(\boldsymbol{\omega}) = \boldsymbol{R}_c(\boldsymbol{\omega}, \theta_a) = r_\mu z_\mu^{\boldsymbol{\kappa}}$, where $\mu \in M$ is an index for which $t_{a.m} = \min(\boldsymbol{t}_a)$. The routine is executed for all θ_a angles of interest. Fig. 1 illustrates the MPA-based post-processing. The algorithm performance is subject to appropriate determination of the setup in terms of K, B, L, and M. The available literature only provides the rule-of-thumb guidelines for their selection (Bekasiewicz et al., 2023; Fourestie & Altman, 2001; Sarkar & Pereira, 1995). Here, however, the MPA setup is determined using the framework outlined in Section 3.

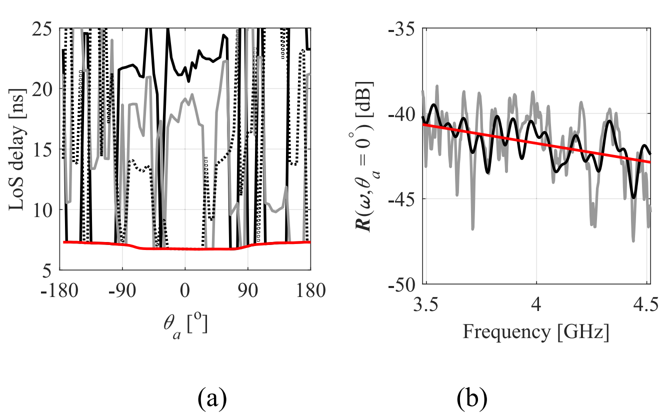

Fig. 1. MPA-based correction: (a) the delay curves extracted using (4) where the red curve at each θ_a corresponds to $\min(\boldsymbol{t}_a)$, as well as (b) the frequency responses before (gray) and after (black) reconstruction using (2). The $\boldsymbol{R}_c(\boldsymbol{\omega}, \theta_a)$ exponent (red) represents the refined response.

3. Surrogate-assisted tuning

The challenges related to determination of appropriate settings for correction algorithm are explained here. Formulation of surrogate-assisted tuning algorithm, as well as discussion of the proposed optimization framework are also provided. The numerical results and discussion are provided in Sections 4 and 5.

3.1. Rule-of-thumb-based setups – challenges

Post-processing performance is subject to appropriate setup of the algorithm. The available literature provides a relatively consistent set of guidelines for determining the parameters based on visual inspection of the test site (Loredo et al., 2004), or the obtained responses (Leon et al., 2009; Soltane et al., 2020) as well as numerical experiments conducted for specific test cases (Bekasiewicz et al., 2023; Sarkar & Pereira, 1995). The setup of MPA is determined based on a combination of engineering-insight with rules-of-thumb. The former refers to estimating the bandwidth B as a proportion of the delay between the LoS signal and its first interference. In (Leon et al., 2009; Loredo et al., 2004; Soltane et al., 2020) determination of the parameter based on visual inspection of the RA-AUT response in the time domain is recommended. The bandwidth is extracted based on the time delay between the peaks of direct and reflected (non-LoS) signals. In (Loredo et al., 2004); B is estimated based on the physical measurements of the RA-AUT distance, as well as the shortest expected path of the reflected signal. Alternatively, estimation of the bandwidth in proportion to the AUT aperture is suggested to ensure higher value of the parameter for small radiators with lower gain (and hence, worsened signal-to-noise) (Bekasiewicz et al., 2023).

Selection of the remaining hyperparameters—arguably due to their less-pronounced effect on correction performance compared to the bandwidth—is limited to simple rules-of-thumb (Leon et al., 2009; Loredo et al., 2004; Sarkar & Pereira, 1995). In (Sarkar & Pereira, 1995), selecting the pencil parameter L between $K/3$ and $K/2$ is suggested. The number of exponentials M in (2) varies from 2 in (Leon et al., 2009) to 4 in (Loredo et al., 2004). The specific values are justified as sufficient for separating noise from LoS responses. Finally, the recommended number of frequency points K is related to the frequency step $\delta\omega$, which vary from sub-MHz in (Soltane et al., 2020) up to a few MHz in (Loredo et al., 2004). Alternatively, in (Bekasiewicz et al., 2023), a lower bound on K at around 201 points is considered as suitable for reliable post-processing.

Insight-based determination of setup poses difficulties in terms of unequivocal identification of the interval between LoS and non-LoS signals (Bekasiewicz et al., 2023). Furthermore, the outlined guidelines concerning the selection of remaining parameters are relatively relaxed which might involve trial-and-error tuning of the algorithm. The latter is difficult, especially given no feedback on quality of the refined responses (the main assumption behind post-processing is lack of, e.g., AC-based measurements). Another (yet associated) challenge involves variability of the optimal setup with frequency of interest f_0, which might necessitate its re-set for each experiment. Illustration of both problems is provided in Fig. 2(a)-(b). It should be emphasized that the difficulties pertinent to reliable identification of interference might result in inconsistency of the extracted LoS-to-non-LoS delays. Demonstration of the problem is shown in Fig. 2(a), where the delays δt vary from 3 ns to 13 ns across f_0, which correspond to the change of estimated bandwidths $B = 1/\delta t$ from 77 MHz to 333 MHz (Leon et al., 2009; Soltane et al., 2020). Significant changes of B with f_0 indicate—contrary to suggestions from, e.g., (Bekasiewicz et al., 2023)—that it needs to be tuned individually w.r.t. each frequency of interest. Finally, Fig. 2(c)-(d) demonstrate that appropriate adjustment of the remaining parameters is required to ensure a high performance of MPA. Challenges related to experience-driven determination of hyperparameters, as well as variation of the optimum setup across test conditions and frequencies

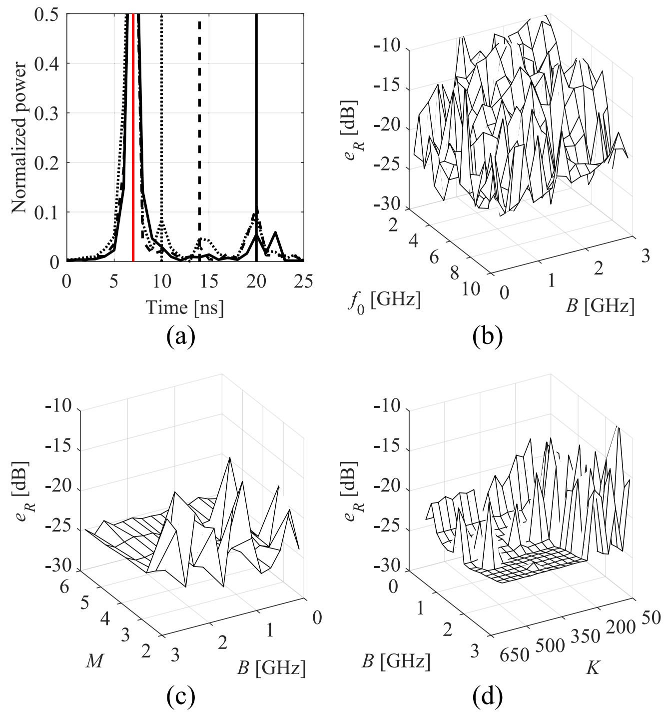

Fig. 2. Manual adjustment of the post-processing setup for the example AUT: (a) determination of the bandwidth based on a delay between the LoS (red) and non-LoS (black) peaks through a visual inspection of the time-domain response at different f_0 frequencies (–), (•••), (– –), and visualization of the e_R (cf. Section 3.2) between the corrected and AC-based responses as a function of: (b) f_0 and B, (c) B and M, as well as (d) B and K.

demonstrate that the problem concerning a reliable post-processing of non-anechoic measurements remains open.

3.2. Surrogate-assisted tuning of hyperparameters

The proposed surrogate-assisted tuning of hyperparameters is realized as a curve-fitting process, where the MPA setup is adjusted so as to minimize the discrepancy between the refined non-anechoic response and the EM simulation results obtained for the given AUT. The challenges associated with the determination of algorithm setup as a result of numerical optimization involve: (i) discrepancies between the far-field responses obtained from the simulations and measurements, as well as (ii) multi-modal and non-differentiable search space (cf. Fig. 2). Fig. 3 illustrates a comparison of EM-based and non-anechoic radiation patterns obtained for the example antennas. The responses vary in terms of angular location and/or the level of the lobes. Here, a surrogate incorporating a non-linear mapping of angular shifts and a uniform scaling between the simulated and the MPA-based responses is used (Koziel, 2010a). The goal is to ensure that the curve fitting process is oriented towards achieving a similar response to the simulated one while retaining the response-specific features resulting from the measurements. A suitable configuration of the MPA parameters is sought as a result of multiple derivative-free optimizations re-set from the starting points that are gradually affected by the already obtained results.

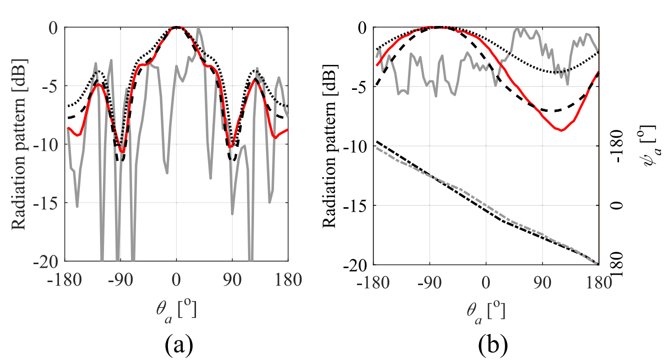

Fig. 3. Non-anechoic radiation patterns (—) before (gray) and after (red) post-processing vs. the EM responses (•••) and EM-based surrogate (– –): (a) a directional antenna at 7 GHz and (b) a compact monopole at 6 GHz. Note that the lines (–•–) in (b) represent a non-linear scaling $\boldsymbol{\Psi}$ of angles obtained for the directional (gray) and the monopole (black) structures.

Let $\boldsymbol{x} = [B\ M\ l\ K]^T$ be the vector of MPA hyperparameters, where l is in relation to K so that $L = Kl$. Then, let $\boldsymbol{R}_c(f_0, \boldsymbol{\theta}) = \boldsymbol{R}_c(\boldsymbol{x}, f_0, \boldsymbol{\theta}) = \boldsymbol{R}_c(\boldsymbol{x})$ be the corrected response obtained using MPA for the given setup $\boldsymbol{x}$. The goal of surrogate-assisted tuning is to obtain the optimum settings $\boldsymbol{x}^*$ for which $\boldsymbol{R}_c$ provides an acceptable approximation of the far-field response from a professional laboratory. Since the latter is not available—as this would contradict the entire concept of non-anechoic (non-AC) measurements—the setup $\boldsymbol{x}^*$ is iteratively approximated (i = 0, 1, …) by solving:

$$\boldsymbol{x}^{(i+1)} = \underset{\boldsymbol{x}}{\operatorname{argmin}}\left(e_R\left(\boldsymbol{R}_c(\boldsymbol{x}), \boldsymbol{R}_s\left(\boldsymbol{x}^{(i)}\right)\right)\right) \tag{5}$$

where $e_R = e_R(\boldsymbol{R}_c(\boldsymbol{x})) = e_R(\boldsymbol{R}_c(\boldsymbol{x}), \boldsymbol{R}_0)$ with $\boldsymbol{R}_0 = \boldsymbol{R}_0(f_0, \boldsymbol{\theta})$, is a root-mean-square error given as:

$$e_R(\boldsymbol{R}_c(\boldsymbol{x})) = \left(\frac{1}{A}\sum_{a=1}^{A}\left(R_0(f_0, \theta_a) - R_c(\boldsymbol{x}, f_0, \theta_a)\right)^2\right)^{0.5} \tag{6}$$

In practice, minimization of (5)—with $\boldsymbol{R}_0 = \boldsymbol{R}_s(\boldsymbol{x}^{(i)})$ used as a reference for the e_R metric—corresponds to a curve-fitting between the reference and corrected far-field characteristics. Here, $\boldsymbol{R}_s$ is a surrogate model adjusted according to $\boldsymbol{R}_c(\boldsymbol{x}^{(i)})$ responses. Let $\boldsymbol{R}_{\text{EM}} = \boldsymbol{R}_{\text{EM}}(f_0, \boldsymbol{\theta})$ denote the EM simulation of the AUT. Then, let $\boldsymbol{\theta}' = [\theta_1' \ldots \theta_{A-1}']^T = [\theta_2 - \theta_1 \ldots \theta_A - \theta_{A-1}]^T$ and $\boldsymbol{t} = [t_1 \ldots t_{A-1}]^T$ be the vectors of the angular steps and their scaling coefficients. The surrogate is of the form:

$$\boldsymbol{R}_s\left(\boldsymbol{x}^{(i)}\right) = \boldsymbol{R}_{\text{EM}}\left(\boldsymbol{\psi}^{(i)}\right)\alpha\left(\boldsymbol{x}^{(i)}\right) \tag{7}$$

where $\boldsymbol{\psi}^{(i)} = [\psi_1^{(i)} \ldots \psi_A^{(i)}]^T = [0\boldsymbol{t}^{(i)} \circ \boldsymbol{\theta}']^T$ (note that "$\circ$" is the Hadamard product) represents the non-linear scaling of $\boldsymbol{\theta}$ obtained through the optimization of $\boldsymbol{t}$ that involves interpolation of $\boldsymbol{R}_{\text{EM}}$ onto $\boldsymbol{R}_c(\boldsymbol{x}^{(i)})$ by solving (in a least-squares sense):

$$\boldsymbol{t}^* = \underset{\boldsymbol{t}}{\operatorname{argmin}}\left(\boldsymbol{R}_{\text{EM}}(\boldsymbol{\psi}) - \boldsymbol{R}_c\left(\boldsymbol{x}^{(i)}\right)\right) \tag{8}$$

Minimization of (8) alters the angular scale of $\boldsymbol{R}_{\text{EM}}$ according to $\boldsymbol{t}^{(i)} = \boldsymbol{t}^*$ so as to minimize its discrepancy w.r.t. $\boldsymbol{R}_c(\boldsymbol{x}^{(i)})$. Note that the process is realized using interpolation (Koziel, 2010a). The uniform scaling coefficient α is given as:

$$\alpha\left(\boldsymbol{x}^{(i)}\right) = \left(\boldsymbol{R}_{EM}\left(\boldsymbol{\psi}^{(i)}\right)^T\boldsymbol{R}_{EM}\left(\boldsymbol{\psi}^{(i)}\right)\right)^{-1}\boldsymbol{R}_{EM}\left(\boldsymbol{\psi}^{(i)}\right)^T\boldsymbol{R}_c\left(\boldsymbol{x}^{(i)}\right) \tag{9}$$

The factor reduces the discrepancy between the EM-based and the corrected responses while retaining the shape of the former. The extracted surrogates are shown in Fig. 3, whereas Fig. 4 demonstrates the effects of extracted input parameters on the shape of the surrogate used for identification of the post-processing setup. It should be emphasized that the goal of uniform scaling (9) is to vertically alter the surrogate model to minimize its discrepancy w.r.t. the corrected non-AC measurements. At the same time, the purpose of (8) is to alter the angular response of $\boldsymbol{R}_s$, prior to its vertical scaling so as to improve the alignment of local minima/maxima of the model against the experimental data from uncontrolled environment.

The starting point $\boldsymbol{x}_0$ in (5) is determined based on the selected lower/upper bounds $\boldsymbol{l}_b/\boldsymbol{u}_b$. At each iteration $i > 0$, $\boldsymbol{x}_0$ is selected as an average of $\boldsymbol{x}^{(i)}$ and $\boldsymbol{x}^{(i-1)}$ designs. At the same time, the surrogate (7) is always extracted w.r.t. $\boldsymbol{x}^{(i)}$. The reasoning behind the "shift" between the

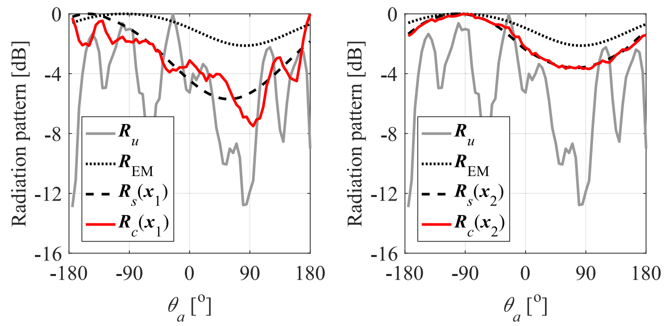

(a) (b)

Fig. 4. The effect of input parameters on the shape of the $R_s(x)$ model obtained for the monopole antenna at 4 GHz frequency: (a) x_1 and (b) x_2. The surrogate in (7) is represented as the EM simulation response modified using non-linear (angle-wise) and uniform scaling factors in (8) and (9), respectively. The process is oriented to align simulations to measurements so as to aid identification of appropriate setup x for post-processing. Note that adjustment of parameters affects not only vertical scale of the model but also shifts radiation minima/maxima.

reference points used for the surrogate extraction and optimization is to re-set (5) each time in the sub-optimal design so as to ensure exploration of the search space towards the refined descent direction. The algorithm can be summarized as follows:

1. Evaluate $\boldsymbol{R}_{EM}$, set $i = 0$, set $\boldsymbol{x}_0 = \boldsymbol{x}^{(0)}$;
2. Extract surrogate (7) at $\boldsymbol{x}^{(i)}$ design;
3. Minimize (5) starting from $\boldsymbol{x}_0$;
4. If $i = 0$ go to step 6; otherwise go to step 5;
5. If $e_R(\boldsymbol{R}_c(\boldsymbol{x}^{(i+1)})) \le e_R{}^*$ END; otherwise go to step 6;
6. Set $e_R{}^* = e_R(\boldsymbol{R}_c(\boldsymbol{x}^{(i+1)}))$, $\boldsymbol{x}^* = \boldsymbol{x}^{(i+1)}$; set $\boldsymbol{x}_0 = (\boldsymbol{x}^{(i+1)} + \boldsymbol{x}^{(i)})/2$, $i = i + 1$, and go to step 2.

In contrast to the existing surrogate-assisted optimization techniques (Bandler, 2004; Koziel, 2010a,b), the goal of the outlined process it to first reduce the discrepancy between the EM-based and uncorrected responses, followed by tuning of the correction parameters to minimize the discrepancy between the modified EM responses and the measurements. The process gradually narrows the gap between the simulations and experimental results, while retaining exploration of the search space (due to multiple optimization restarts). Furthermore, a combination of non-linear and uniform scaling compensates not only for the generic discrepancy between signal amplitudes but also for misalignment of local minima (e.g., due to shift in radiation nulls). The main motivation behind the approach is the discrepancy (due to model simplifications) between the EM simulations and measurements that cannot be unequivocally corrected based on high-fidelity measurements (e.g., performed in an AC environment). As already explained, availability of such data would challenge the entire concept of post-processing noisy far-field responses.

It should be reiterated that, due to highly multi-modal character of the search space and mixed-integer nature of the problem, minimization of (5) is realized using a derivative-free algorithm. Here, a pattern search method is used (Conn et al., 2009; Koziel, 2010b). To mitigate the risk of getting stuck in poor local optima, the proposed routine is embedded within the framework that re-sets the optimization from a few starting points.

3.3. Optimization framework

Let $\boldsymbol{X}_s = \{\boldsymbol{x}_{s.1}, \ldots, \boldsymbol{x}_{s.P}\}$ be a set of $P = 2D + 1$ (where D is dimensionality of $\boldsymbol{x}$) starting points generated using a star-distribution design of experiment and scaled according to the modified lower and upper bounds $\boldsymbol{l}_b' = \boldsymbol{l}_b + \boldsymbol{d}_0$ and $\boldsymbol{u}_b' = \boldsymbol{u}_b - \boldsymbol{d}_0$, where $\boldsymbol{d}_0 = (\boldsymbol{u}_b - \boldsymbol{l}_b)/\beta$ (here, $\beta = 5$ to ensure that the designs are not located at the search space edges) (Bandler et al., 2004). The framework for optimization of the MPA setup can be summarized as follows:

1. Set $\boldsymbol{l}_b$, $\boldsymbol{u}_b$, generate $\boldsymbol{X}_s$, set $p = 1$;
2. Set $\boldsymbol{x}^{(0)} = \boldsymbol{x}_{s.p}$, find $\boldsymbol{x}_p{}^*$ and $e_{R.p}{}^*$ by solving (5);
3. Include $\boldsymbol{x}_p{}^*$ and $e_R{}^*$ to $\boldsymbol{X}^*$ and $\boldsymbol{E}_R{}^*$ sets, respectively;
4. If $p < P$, set $p = p + 1$ and go to Step 2; otherwise set $\boldsymbol{x}^* = \boldsymbol{x}_\gamma{}^*$, where γ represents an index from $\boldsymbol{X}^*$ for which $e_{R.}^{\gamma}{}^* = \min\{\boldsymbol{E}_R{}^*\}$, END.

The design $\boldsymbol{x}^*$ obtained using the above routine represents optimal configuration of parameters for the MPA at the given center frequency f_0. It is worth emphasizing that the proposed routine is generic. Given availability of non-anechoic measurements with suitably small $\delta\omega$, the framework can be used with other multi-frequency correction algorithms. Here, the application is limited to the matrix-pencil routine due to its reliance on a relatively large number of mixed-integer control parameters. Integration of the method with other algorithms will be considered elsewhere.

It is worth noting that the convergence of the optimization is ensured by the implementation of pattern search method (Conn et al., 2009; Koziel, 2010b). In other words, the algorithm seeks for the optimum configuration of the hyperparameters through exploration of the search space on a finite grid. Once no further improvement is possible, grid granularity is increased to further exploit the identified region. The optimization is terminated once no improvement is possible or the maximum number of iterations is achieved. The latter is important to ensure identification of hyperparameters at a manageable computational cost. As already mentioned, the risk of getting stuck in poor optima is mitigated by multiple re-starts of the algorithm from a set of starting points on the grid. Nonetheless, identification of a global optimum is not guaranteed. On the other hand, deterministic nature of the proposed framework makes it ideal for ensuring consistently repeatable optimization results.

4. Results

The presented framework has been benchmarked using two antenna structures shown in Fig. 5, i.e., an antipodal Vivaldi and a compact spline-based monopole (Bekasiewicz et al., 2023). The measurements have been performed in two non-anechoic sites with dimensions of 8.4 × 4.5 × 3.1 m^3 (room A) and 5.5 × 4.5 × 3.1 m^3 (room B), respectively. Both sites are regular office rooms not tailored to far-field experiments, except for the installation of the necessary gear (cf. Fig. 6), i.e., positioning towers, a vector network analyzer, suitable cables, and adapters (Bekasiewicz et al., 2023). For each test, the Vivaldi antenna has been used as the RA. The angular resolution for AUT rotation is set to 5°, which translates to a total of 72 measurements for a full 360° radiation pattern in a single plane. The lower and upper bounds on the B M l K parameters are set to $\boldsymbol{l}_b = [0.1\ 2\ 1/3\ 101]^T$ and $\boldsymbol{u}_b = [3\ 5\ 0.5\ 601]^T$ (cf.

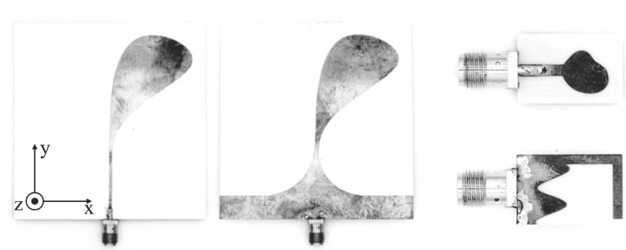

(a) (b)

Fig. 5. Photographs of the antennas used for experiments: (a) antipodal Vivaldi and (b) spline monopole. The radiators are not in scale.

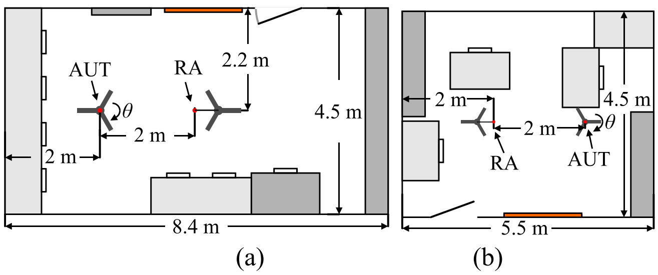

Fig. 6. Test sites: (a) A and (b) B. Light- and dark-gray rectangles represent the short and tall furniture. The red dots denote the RA and AUT locations on the measurement towers, whereas θ indicates the direction of AUT rotation. Orange stripes represent the metallic whiteboards (contributors to strong signal interference (Bekasiewicz et al., 2023)).

Section 3.2). The maximum number of iterations for the pattern search algorithm is limited to 50.

The MPA, coupled with automatic tuning, has been compared in terms of performance against the results obtained using rules-of-thumb-based setups from the literature (Bekasiewicz et al., 2023; Leon et al., 2009; Loredo et al., 2004). For the method (i), the bandwidth is estimated based on the minimum time-domain delay between the LoS transmission and the first reflected signal, whereas the number of points is determined from the suggested frequency step size of $\delta\omega = 5$ MHz (Loredo et al., 2004). The number of exponentials and the pencil parameter are set to $M = 4$ and $L = 5/12\ K$ which represents an average of the recommended range (cf. Section 3.1). For the method (ii), the bandwidth os selected as twice the LoS-to-non-LoS delay along with $M = 2$ and $\delta\omega = 2.5$ MHz (Leon et al., 2009). Due to lack of explicit discussion on L, the parameter has been set to the same value as in (Loredo et al., 2004). Finally, the method (iii)—originally formulated for time-domain measurements (Bekasiewicz et al., 2023)—relates the bandwidth to the antenna aperture C as $B \geq \upsilon(3C)^{-1}$ (υ is the speed of light), while limiting the number of points around f_0 to $K = 201$. The setup of parameters L and M has been adopted from (Loredo et al., 2004). The performance of post-processing is evaluated in terms of e_R, calculated with respect to the measurements of the considered antennas in the anechoic chamber ($\boldsymbol{R}_0 = \boldsymbol{R}_{\mathrm{AC}}$; cf. Section 3.2).

4.1. Antipodal Vivaldi antenna

The first case study concerns non-AC measurements of the antipodal Vivaldi antenna radiation patterns in the yz-plane (cf. Fig. 5) at the following frequency points $\boldsymbol{f}_0 = \{3\ 4\ 5\ 6\ 7\ 8\ 9\ 10\ 11\ 12\}$ GHz. To enable high-granularity adjustment of the MPA setup, a total of 24,001 data points representing transmission within the RA-AUT system per θ_a angle—over the frequency range from 1.5 GHz to 13.5 GHz—are used. Once the measurements are performed, optimum MPA setups are extracted using the framework of Section 3.3.

The correction has also been realized using the MPA with rule-of-thumb settings. For the method (i), B is estimated as a result of visual inspection of the RA-AUT power response at $\theta_a = 0°$ (obtained using an inverse Fourier transform (Oppenheim & Schafer, 2009); cf. Fig. 2(a)) in order to identify the occurrence of the LoS peak and the first interference. The estimated bandwidths for rooms A and B are $B_A = 1/\delta t = (12\ \mathrm{ns} - 6.5\ \mathrm{ns})^{-1} = 0.18$ GHz and $B_B = 0.2$ GHz, respectively. The remaining parameters are set as explained in Section 4. The resulting setups are $\boldsymbol{x}_A^{(\mathrm{i})} = [0.18\ 4\ 5/12\ 37]^T$ and $\boldsymbol{x}_B^{(\mathrm{i})} = [0.2\ 4\ 5/12\ 41]^T$. The settings for method (ii) are $\boldsymbol{x}_A^{(\mathrm{ii})} = [0.36\ 2\ 5/12\ 145]^T$ and $\boldsymbol{x}_B^{(\mathrm{ii})} = [0.4\ 2\ 5/12\ 161]^T$. Finally, given that the Vivaldi aperture is $C \approx 0.1$ m, $B = 1$ GHz is obtained for the method (iii) and the resulting setup is $\boldsymbol{x}^{(\mathrm{iii})} = [1\ 4\ 5/12\ 201]^T$ (the same for both sites).

The performance of MPA-based correction for both test sites is summarized in Tables 1 and 2, respectively. The results indicate a notable variations of the post-processing setups as a function of frequency and test site. The optimized bandwidths span from $B = 0.11$ GHz (site A; $f_0 = 10$ GHz) to $B = 2.42$ GHz (site A; $f_0 = 8$ GHz), while the number of frequency points range from $K = 110$ (A; at 9 GHz) to $K = 595$ (B; at 10 GHz). The remaining variables exhibit changes across the defined $\boldsymbol{l}_b$ and $\boldsymbol{u}_b$ bounds. The errors e_R—averaged over all of the considered frequencies—amount to –23.6 dB and –23 dB for sites A and B, which translates to improvement of the radiation patterns fidelity (w. r.t. the AC-based measurements) by 7.7 dB and 8.8 dB, respectively. At the same time, the correction using the benchmark setups improves the quality of responses by 3.9 dB to 7.3 dB for site A and 5.4 dB to 8.9 dB for the second room. Overall, compared to the manual setups, the performance improvement due to the automatic MPA is from 0.4 dB to 3.9 dB for room A and up to 3.4 dB for site B.

The radiation patterns obtained in both sites at the selected frequencies are shown in Fig. 7. The discrepancies between the corrected responses are minor and highly resemble the AC-based measurements. At the same time, the fidelity of the refined characteristics is substantially improved compared to the uncorrected data. Furthermore, the results gathered in Tables 1 and 2 demonstrate that, for the given antenna and the frequency of interest, the correction parameters optimized for each test site are different. It is worth noting, however, that the quality of correction is slightly deteriorated around the sidelobes. The results are supported by the cumulative Pearson correlation r^2 (i.e., evaluated over all frequencies of interest) obtained for the AC-based

Table 1
Vivaldi – MPA correction performance (test site A).

f_0 [GHz]	Automatic adjustment of algorithm setup							Benchmark methods		
	non-AC	MPA parameters				Corrected		(i)	(ii)	(iii)
	$e_R(\boldsymbol{R}_u)$[dB]	B	M	l	K	$e_R(\boldsymbol{R}_c)$[dB]	Δ*[dB]	$e_R(\boldsymbol{R}_c)$[dB]	$e_R(\boldsymbol{R}_c)$[dB]	$e_R(\boldsymbol{R}_c)$[dB]
3	–12.35	0.33	3	0.45	507	–24.36	12.0	–21.14	**–24.47**$	–23.84
4	–20.16	1.03	5	0.48	425	**–31.26**	11.1	–29.81	–17.33	–31.02
5	–16.79	0.94	5	0.35	195	–22.14	5.35	–20.20	–17.28	**–22.19**
6	–11.53	0.16	2	0.43	543	–18.72	7.19	–18.07	**–19.28**	–19.05
7	–17.48	1.29	4	0.39	190	**–24.72**	7.24	–23.63	–22.10	–24.70
8	–18.33	2.42	4	0.36	584	**–23.97**	5.64	–22.61	–13.13	–22.87
9	–15.95	0.74	3	0.44	110	**–23.35**	7.40	–22.31	–21.95	–23.07
10	–15.68	0.11	3	0.36	242	–22.25	6.57	**–22.48**	–22.20	–21.61
11	–16.78	1.55	2	0.38	381	**–24.05**	7.27	–19.72	–20.81	–22.27
12	–13.45	1.07	2	0.41	284	**–20.75**	7.30	–18.04	–18.44	–20.59
E#	–15.85	–	–	–	–	**–23.56**	7.71	–21.80	–19.70	–23.12
$E(\Delta)$	–	–	–	–	–	**7.71**	–	5.95	3.85	7.27

* Calculated as $\Delta = e_R(\boldsymbol{R}_u(f_0, \boldsymbol{\theta})) - e_R(\boldsymbol{R}_c(f_0, \boldsymbol{\theta}))$.
# E represents an average over all considered frequencies.
$ The best obtained responses are bold.

Table 2
Vivaldi – MPA correction performance (test site B).

f_0 [GHz]	Automatic adjustment of algorithm setup							Benchmark methods		
	non-AC	MPA parameters				Corrected		(i)	(ii)	(iii)
	$e_R(R_u)$[dB]	B	M	l	K	$e_R(R_c)$[dB]	Δ^*[dB]	$e_R(R_c)$[dB]	$e_R(R_c)$[dB]	$e_R(R_c)$[dB]
3	–12.80	0.42	5	0.48	395	–22.92	10.1	**–23.67**$^{\$}$	–23.49	–23.13
4	–14.65	1.29	5	0.50	162	–28.06	13.4	–25.55	–17.05	**–28.95**
5	–10.69	1.26	4	0.36	251	–20.78	10.1	–16.45	–16.86	**–22.03**
6	–11.67	0.58	2	0.45	251	**–19.24**	7.57	–13.46	–15.74	–16.69
7	–15.22	0.83	5	0.49	544	**–25.04**	9.82	–22.91	–23.44	–24.97
8	–15.74	1.29	2	0.40	201	–23.49	7.75	–24.85	–22.01	**–25.21**
9	–16.09	1.26	4	0.38	373	–23.85	7.76	**–24.65**	–24.51	–24.36
10	–15.36	0.50	3	0.41	595	–22.74	7.38	–22.73	**–23.12**	–22.24
11	–13.85	0.68	3	0.34	547	–22.82	8.97	–21.65	–15.16	**–22.91**
12	–15.52	1.55	3	0.48	440	**–20.76**	5.24	–19.16	–14.36	–19.90
$E^{\#}$	–14.16	–	–	–	–	–22.97	8.81	–21.51	–19.57	**–23.04**
$E(\Delta)$	–	–	–	–	–	8.81	–	7.35	5.42	**8.88**

$^{\#,*,\$}$ see Table 1.

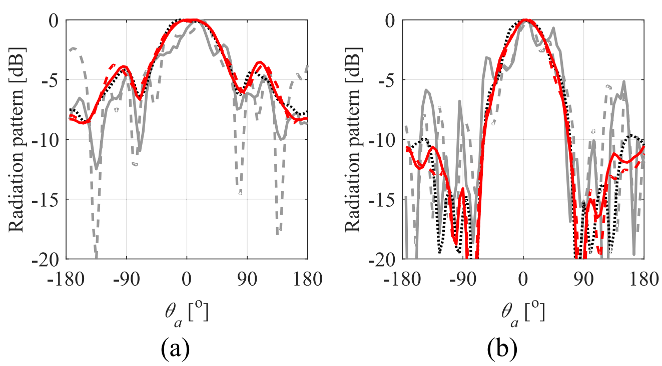

Fig. 7. Vivaldi antenna – radiation patterns obtained in test site A (–) and B (– –) before (gray) and after (red) MPA post-processing vs. AC-based measurements (•••) at: (a) 4 GHz and (b) 7 GHz frequencies.

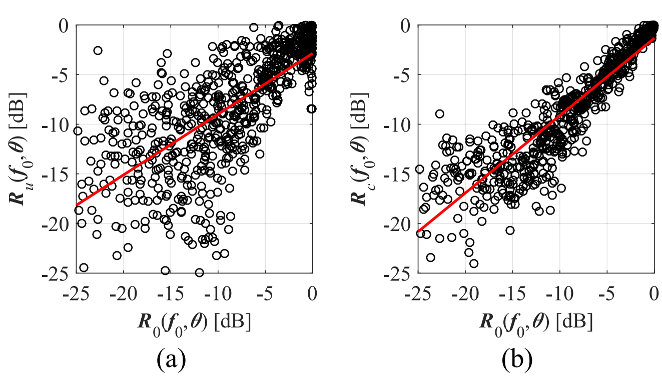

Fig. 8. Vivaldi antenna – non-anechoic vs. AC measurements (site A): (a) before (average $r^2 = 0.44$) and (b) after automatic MPA correction (average $r^2 = 0.81$). Red line denotes a linear regression of data.

data and the non-anechoic responses before, and after the MPA post-processing (see Fig. 8). Although the correction substantially improves the quality of responses, an increased spread of points for low-decibel values can still be observed. The effect stems from the positioning errors of the AUT, deteriorated signal-to-noise ratio for faint signals propagating in the challenging conditions, as well as the differences in the test gear used for experiments (cf. Section 5.4). Nonetheless, for the considered sites and frequencies, the MPA with surrogate-assisted tuning of hyperparameters outperforms the rule-of-thumb based setups in terms of correction performance while not relying on engineering insight.

4.2. Compact spline-based monopole

The second case study involves the MPA-based correction of the monopole antenna measurements in yz-plane (cf. Fig. 5). The frequencies of interest are $\boldsymbol{f}_0 = \{3\ 3.5\ 4\ 4.5\ 5\ 5.5\ 6\ 6.5\ 7\ 7.5\}$ GHz. The non-AC measurements comprising a total of 14,001 points per θ_a angle spanned over a range from 2 GHz to 9 GHz have been used. The post-processing setups have been adjusted using the algorithm of Section 3.3. The benchmark methods parameters have been set as explained above. The estimated peak-to-peak delays are from 6.5 ns to 9 ns and from 6.5 ns to 8.5 ns for sites A and B, respectively. The settings extracted for methods (i) and (ii) are: $\boldsymbol{x}_A^{(\mathrm{i})} = [0.4\ 4\ 5/12\ 81]^T$, $\boldsymbol{x}_B^{(\mathrm{i})} = [0.5\ 4\ 5/12\ 101]^T$ and $\boldsymbol{x}_A^{(\mathrm{ii})} = [0.8\ 2\ 5/12\ 321]^T$, $\boldsymbol{x}_B^{(\mathrm{ii})} = [1\ 2\ 5/12\ 401]^T$. For the method (iii), the monopole aperture is $C \approx 0.03$ m, hence the estimated bandwidth is $B = 3$ GHz and the setup is $\boldsymbol{x}^{(\mathrm{iii})} = [3\ 4\ 5/12\ 201]^T$.

Tables 3 and 4 summarize the post-processing results using the MPA with automatic and rule-of-thumb setups. Similarly to Vivaldi antenna, the framework of Section 3 generates high-fidelity responses (compared to AC-based data). The optimized bandwidths span from 0.52 GHz (site A; at 7.5 GHz) to 3 GHz (B; at 6.5 GHz), whereas the number of frequency points used for correction ranges from 151 (A; at 4 GHz) to 481 (B; at 7.5 GHz). The average e_R errors are –23.9 dB and –26.6 dB, which translates to improvement of fidelity by 12.4 dB and by 14.4 dB (w.r.t. raw data) in site A and B, respectively. At the same time, the quality of MPA correction for the benchmark methods ranges from 6.9 dB to 11.4 dB (site A) and from 6.1 dB to 12.3 dB (site B). Overall, the MPA with automatic tuning offers from 1 dB to 5.4 dB (A) and from 2.1 dB to 8.3 dB (B) higher performance compared to the rule-of-thumb setups.

The radiation patterns at selected frequencies are shown in Fig. 9, whereas the correlations between AC and non-anechoic responses are visualized in Fig. 10. The discrepancies between the refined and AC-based measurements are minor (regardless of the test site), especially given a substantial improvement compared to the uncorrected characteristics. Outliers in Fig. 10(b) are associated with the responses extracted at the 7.5 GHz frequency for which the MPA underperforms regardless of the hyperparameters setup (see Section 5 for a discussion on the problem). Notwithstanding, the average improvement of the refined characteristics is substantial (also when compared to the results obtained for the Vivaldi antenna). Again, the MPA with automatic tuning outperforms the implementations with rule-of-thumb setups in terms of performance. It should be noted that for the spline monopole, the fidelity improvement resulting from using the proposed framework is notably higher than for the Vivaldi, suggesting that automatic tuning is especially useful for non-AC tests of compact, low-gain radiators.

Table 3
Monopole – MPA correction performance (test site A).

f_0 [GHz]	Automatic adjustment of algorithm setup							Benchmark methods		
	non-AC	MPA parameters				Corrected		(i)	(ii)	(iii)
	$e_R(R_u)$[dB]	B	M	l	K	$e_R(R_c)$[dB]	Δ^{*}[dB]	$e_R(R_c)$[dB]	$e_R(R_c)$[dB]	$e_R(R_c)$[dB]
3.0	–11.79	2.71	5	0.37	384	–24.94	13.15	–13.91	**–25.56**$^{\$}$	–24.62
3.5	–9.74	0.94	5	0.36	318	**–25.84**	16.10	–15.96	–20.25	–24.46
4.0	–12.42	2.02	5	0.37	151	**–31.32**	18.90	–15.92	–29.63	–29.55
4.5	–8.28	1.55	2	0.45	401	–25.62	17.34	–23.77	–24.56	**–25.72**
5.0	–15.88	1.36	5	0.38	284	–23.38	7.50	–23.02	**–24.85**	–24.31
5.5	–12.91	1.26	2	0.35	418	**–26.55**	13.64	–23.29	–26.06	–23.80
6.0	–10.06	1.00	2	0.47	262	**–29.78**	19.72	–21.41	–23.85	–29.00
6.5	–14.56	1.84	4	0.40	451	**–27.06**	12.50	–22.39	–21.26	–23.21
7.0	–12.01	0.74	2	0.49	223	–14.56	2.55	–14.08	**–14.91**	–14.16
7.5	–7.77	0.52	4	0.50	227	–9.85	2.08	**–10.90**	–9.04	–10.14
$E^{\#}$	–11.54	–	–	–	–	**–23.89**	12.35	–18.47	–22.00	–22.90
$E(\Delta)$	–	–	–	–	–	**12.35**	–	6.92	10.46	11.36

$^{\#,*,\$}$ see Table 1.

Table 4
Monopole – MPA correction performance (test site B).

f_0 [GHz]	Automatic adjustment of algorithm setup							Benchmark methods		
	non-AC	MPA parameters				Corrected		(i)	(ii)	(iii)
	$e_R(R_u)$[dB]	B	M	l	K	$e_R(R_c)$[dB]	Δ^{*}[dB]	$e_R(R_c)$[dB]	$e_R(R_c)$[dB]	$e_R(R_c)$[dB]
3.0	–8.82	2.13	4	0.38	251	**–27.06**$^{\$}$	18.24	–14.19	–26.59	–23.76
3.5	–8.65	1.16	5	0.43	371	**–25.84**	17.19	–18.33	–23.77	–22.12
4.0	–8.82	1.55	2	0.33	334	**–35.17**	26.35	–16.38	–30.46	–24.32
4.5	–16.31	2.71	3	0.36	351	**–32.79**	16.48	–21.13	–32.43	–33.51
5.0	–14.25	1.74	3	0.45	387	**–29.15**	14.90	–22.94	–27.73	–26.32
5.5	–13.73	1.36	5	0.36	303	–25.65	11.92	–19.90	**–28.69**	–27.64
6.0	–9.82	0.68	4	0.34	433	–23.47	13.65	–13.62	**–24.82**	–21.90
6.5	–13.43	3.00	3	0.42	232	–20.50	7.07	–15.46	–19.78	**–20.53**
7.0	–12.83	2.42	4	0.46	384	**–31.17**	18.34	–28.80	–15.60	–27.58
7.5	–15.73	1.00	4	0.45	481	–15.19	0.54	–12.48	**–15.20**	–14.53
$E^{\#}$	–12.24	–	–	–	–	**–26.60**	14.36	–18.32	–24.51	–24.22
$E(\Delta)$	–	–	–	–	–	**14.36**	–	6.08	12.27	11.98

$^{\#,*,\$}$ see Table 1.

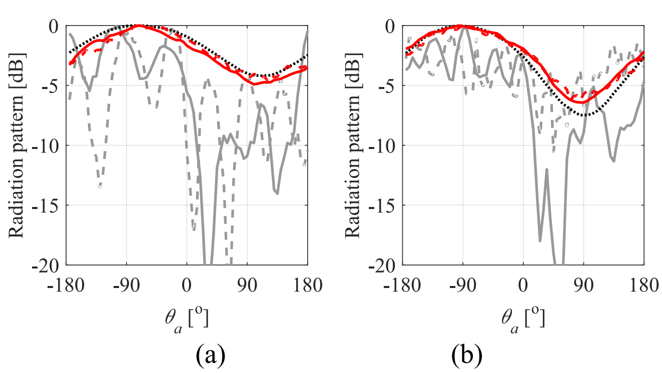

Fig. 9. Monopole antenna – radiation patterns from test sites A (–) and B (– –) before (gray) and after (red) post-processing vs. AC-based measurements (•••) at: (a) 3.5 GHz and (b) 5.5 GHz frequencies.

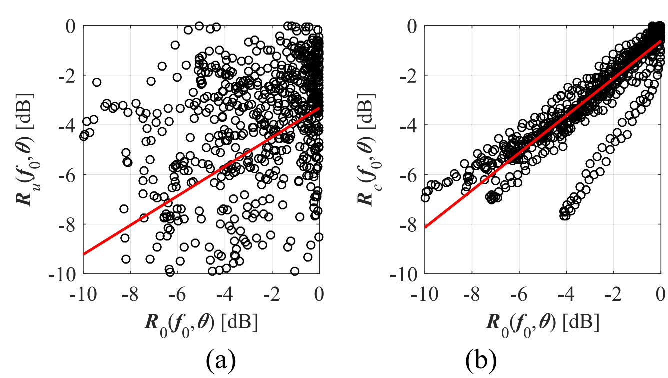

Fig. 10. Monopole – non-anechoic vs. AC measurements (site B): (a) before (average $r^2 = 0.25$) and (b) after automatic MPA correction (average $r^2 = 0.98$). Red line denotes the linear regression of data.

5. Discussion and comparisons

A discussion of the method with focus on the measurement inaccuracy and the computational cost of the post-processing is provided here along with comparisons of the presented algorithm against the benchmark routines. It is worth noting that analysis of the post-processing robustness to the measurement uncertainties is not considered as it exceeds the scope of the work. For more information on the effects of uncertainties and environmental dynamics on the correction performance of non-anechoic experiments, see (Bekasiewicz & Waladi, 2024; Bekasiewicz et al., 2023; Kurokawa et al., 2009).

5.1. *MPA – automatic vs. manual setup*

The results gathered in Tables 3 and 4 indicate that, for the monopole antenna, the proposed correction framework offers a substantial improvement of the responses fidelity compared to the MPA with rule-of-thumb-based responses (w.r.t. AC measurements). Notwithstanding, the method does not guarantee that the lowest e_R errors will be obtained across all of the considered frequencies (cf. Section 3.3). On the other hand, it generates the best responses for most of them. For the remaining ones, the best correction results are scattered between the benchmark MPA realizations. The data obtained for the monopole suggest to support the claim that a one-fit-all manual setup that provides the best responses does not exist.

As it comes to the Vivaldi structure, the data gathered in Tables 1 and 2 demonstrate that, for the site A, the MPA with automatically obtained setup outperforms the manually tuned ones at most of the frequencies (while for the remaining ones—similarly as for the monopole—the best-fit responses are scattered across the available setups). However, for the site B, the automatic tuning is outperformed (albeit slightly) by the benchmark method (iii) which offers from 0.1 dB (at 11 GHz) to 1.7 dB (at 8 GHz) better correction responses. One should note that the averaged e_R error for the approach (iii) is 0.1 dB lower compared to the one based on automatic tuning.

The obtained responses demonstrate that the objective function for setup optimization that evaluates the discrepancy between the corrected response and its corresponding EM simulation might represent a bottleneck of the proposed framework. In other words, the method is based on the assumption that the EM results and measurements should be similar (shape-wise), which might not be the case for complex radiation patterns featuring, e.g., several side lobes. The outlined problem is demonstrated in Fig. 11, where the comparisons of measurements (performed in both AC and non-AC conditions) against the EM simulations are provided. The obtained characteristics show that, although the Vivaldi responses are similar, the discrepancy between the EM simulations and the AC-based data (resulting, e.g., from the manufacturing tolerances, manual assembly, and/or the effects of the test gear on the measurements performance; cf. Section 5.4) is noticeable. From this perspective, the algorithm is biased towards matching the corrected radiation pattern to the EM simulation responses. The mentioned aspect tend to be of a lesser concern for omnidirectional structures (as the radiator of Section 4.2) due to their (predominantly) “smoother” responses (cf. Fig. 9).

Regardless of the discussed limitation, the most important feature of the proposed framework is that it is unassuming. In other words, the correction can be performed by an inexperienced engineer, and its quality will depend only on the results of deterministic optimization (and the performance discrepancy between the simulation data and measurements of the antenna prototype). At the same time, for the rule-of-thumb routines, the fidelity of the results depends on a manual (and hence biased) determination of the site-specific setups, which makes the process prone to failure. Furthermore, the results seem to support the claim that the proposed automatic optimization of the MPA hyper-parameters, while incapable of ensuring globally optimum patterns, offers an acceptable compromise between the quality of responses and engineering insight required for their determination, or (more appropriately) lack of thereof.

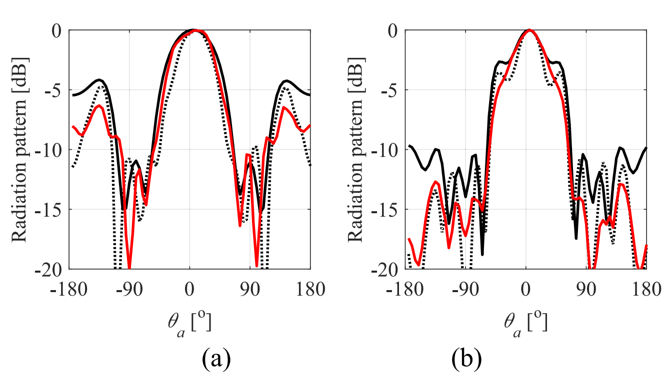

Fig. 11. Test site B – Vivaldi antenna patterns obtained from EM simulations (—), AC measurements (•••), and corrected non-AC data (red) at: (a) 5 GHz, and (b) 8 GHz frequencies. Note that alignment of refined data to simulations within ± 90° to ± 180° range (e.g., in terms of peak shifts) negatively affects e_R metric due to discrepancy between EM and AC-based data.

5.2. Benchmark against other post-processing routines

To provide an additional insight into the fidelity of post-processing results, the proposed framework has been compared against the state-of-the-art routines, i.e., (1) the time-gating algorithm with an adaptive composite window and (2) a Hann-based kernel, (3) the approach based on the complex-value implementation of Morlet wavelets, as well as (4) an algorithm that exploits the discrete prolate spheroidal sequences (DPSS) for correction (de Sao Jose et al., 2020; Soltane et al., 2020; Bekasiewicz & Waladi, 2024; Dzwonkowski & Bekasiewicz, 2024). The performance for all of the considered algorithms rely on manual setup of the bandwidth and the number of frequency points around the specific f_0. Given that, in Section 4, the best rule-of-thumb-based results have been obtained for the setup (iii), i.e., $K = 201$, as well as $B = 1$ GHz (for Vivaldi) and $B = 3$ GHz (for monopole), the mentioned parameters have been re-used for the considered tests. All of the experiments have been performed using the same sets of frequencies as in Section 4.

The results gathered in Table 5 (for the Vivaldi structure) express the post-processing performance in terms of the average e_R error E, e_R median M, as well as their change with respect to the uncorrected non-anechoic responses, i.e., $E(\Delta)$ and $M(\Delta)$. The data indicate that, for the site A, the MPA enhanced using the proposed framework outperforms the benchmark algorithms in terms of the considered metrics. The improvement of the average and median performance figures vary from 0.4 dB to 3.5 dB and from 1.1 dB to 4 dB for the manual MPA and the method (de Sao Jose et al., 2020), respectively. For the site B, the Morlet and DPSS methods offer the best results in terms of the average (9.1 dB) and median (8.4 dB) correction, respectively. It is worth noting, however, that the differences are relatively small and amount to just 0.3 dB and 0.4 dB in favor of the former and latter, respectively.

Table 6 demonstrates the results obtained for the monopole antenna. For the site A, the automatic MPA outperforms competitive algorithms by up to 8.5 dB and 9.8 dB in terms of the average and median (as compared to (de Sao Jose et al., 2020). Similarly, for the site B, the correction performance is up to 10.3 dB and 9.8 dB better compared to (de Sao Jose et al., 2020). It is also worth noting that the median response in site A is over 1.8 dB better compared to the average, which is due to the presence of outliers at 7 GHz and 7.5 GHz frequencies characterized by the poor performance (both before and after correction), especially when compared against the responses from site B (cf. Tables 3 and 4). The obtained deterioration of correction performance is reflected by poor quality of the responses obtained in Tables 3 (at 7 GHz and 7.5 GHz, respectively) and IV (at 7.5 GHz). The observed discrepancies stem from site-to-site test gear differences. More in-depth discussion on the problem is given in Section 5.4.

Finally, it is apparent that the performance of algorithm (de Sao Jose et al., 2020) is inferior for both antennas and test sites, whereas the method (Soltane et al., 2020) generates much better responses for the monopole than for Vivaldi. The reason is that both algorithms involve rudimentary mechanisms for identification of the kernel function intervals, i.e., based either on static thresholds (de Sao Jose et al., 2020) or visual inspection of the impulse response (Soltane et al., 2020). Much better performance of the latter for the omnidirectional antenna stems from (relatively) steady LoS peak delays as a function of the RA-AUT angular positions, which is not the case for the Vivaldi. In contrast, the algorithms of (Bekasiewicz & Waladi, 2024) and (Dzwonkowski & Bekasiewicz, 2024) employ a holistic analysis of impulse responses to ensure appropriate centering of the kernels w.r.t. useful fractions of the RA-AUT signals. It should be reiterated that the mechanism for automatic identification of the components that correspond to LoS transmission is an inherent part of the MPA implementation. For more comprehensive discussion the effects of the LoS delay changes on antenna correction performance, see (Bekasiewicz & Waladi, 2024; Bekasiewicz et al., 2023).

Table 5
Vivaldi – MPA correction vs. state-of-the-art algorithms.

	Uncorrected		Corrected using post-processing methods					
		$\boldsymbol{R}_u$	(1)	(2)	(3)	(4)	MPA (iii)	This work
Site A	E#	–5.85	–20.04	–21.40	–22.86	–22.96	–23.12	**–23.56** %
	M*	–16.37	–19.66	–21.30	–22.14	–22.35	–22.57	**–23.66**
	$E(\Delta)$$	–	4.19	5.55	7.01	7.11	7.27	**7.71**
	$M(\Delta)$$	–	3.29	4.94	5.77	5.98	6.21	**7.30**
Site B	E#	–14.16	–16.82	–17.06	**–23.26**	–23.20	–23.04	–22.97
	M*	–14.94	–16.42	–16.78	**–22.91**	–23.29	–23.02	–22.87
	$E(\Delta)$$	–	2.66	2.90	**9.10**	9.04	8.88	8.81
	$M(\Delta)$$	–	1.48	1.84	**7.98**	8.35	8.09	7.94

E represents an average over all considered frequencies.
* M represents median over all frequencies of interest.
$ Calculated (for the given method) as $\Delta = e_R(\boldsymbol{R}_u(f_0, \boldsymbol{\theta})) - e_R(\boldsymbol{R}_c(f_0, \boldsymbol{\theta}))$.
% The best obtained responses are bold.

Table 6
Monopole – MPA correction vs. state-of-the-art algorithms.

	Uncorrected		Corrected using post-processing methods					
		$\boldsymbol{R}_u$	(1)	(2)	(3)	(4)	MPA (iii)	This work
Site A	E#	–11.54	–15.44	–20.86	–23.61	–23.72	–22.9	**–23.89** %
	M*	–11.90	–15.91	–22.34	–23.64	–22.95	–24.39	**–25.73**
	$E(\Delta)$$	–	3.90	9.31	12.06	12.18	11.36	**12.35**
	$M(\Delta)$$	–	4.01	10.44	11.74	11.05	12.49	**13.83**
Site B	E#	–12.24	–16.27	–22.93	–22.82	–22.10	–24.22	**–26.60**
	M*	–13.13	–16.63	–22.67	–23.88	–22.71	–24.04	**–26.45**
	$E(\Delta)$$	–	4.03	10.69	10.58	9.86	11.98	**14.36**
	$M(\Delta)$$	–	3.50	9.54	10.75	9.58	10.91	**13.32**

#,*,$,% see Table 5.

5.3. Deterministic vs. stochastic optimization of hyperparameters

The performance of pattern search solver incorporated within the proposed framework are compared against two stochastic methods, i.e., Bayesian optimization (BO) and genetic algorithm (GA) (Eiben & Smith, 2015; Garnett, 2023). The former maximizes the expected improvement in order to balance the exploration and exploitation. The genetic algorithm implements standard mechanisms such as tournament selection, Gaussian mutation, and elitism (Eiben & Smith, 2015). Population size and number of generations are set to 50 and 10, respectively. The post-processing results obtained using the considered routines, and gathered in Table 7, indicate that the proposed deterministic method outperforms benchmark algorithms for all but one test case. Overall, the average improvement of optimization performance in the site A is up to 1.4 dB and 1.19 dB for the monopole and Vivaldi, respectively. In the site B, the deterministic method offers notable improvement of correction fidelity (up to almost 2 dB) for the monopole. However, for the Vivaldi, the algorithm is outperformed (albeit slightly, the average discrepancy amounts to just 0.02 dB) by GA optimizer. Furthermore, a relatively poor performance of BO, may stem from the difficulties related to identification of an accurate data-driven representation of the functional landscape using Gaussian process regression (see Fig. 2).

Regardless of the obtained results, stochastic nature of the benchmark methods makes the obtained responses subject to change between consecutive runs. Conversely, the pattern search optimization is deterministic, which ensures consistency of the optimization results. A more in-depth evaluation of the optimization performance would require analyses of stochastic algorithms performance. The problem, however, is beyond the scope of this work and will be considered elsewhere.

5.4. Effects of used test-gear on repeatability of measurements

The problem concerning deterioration of the corrected non-AC responses when compared against the AC measurements can be attributed to differences between the test gear used in experiments (both in the AC, but also between the test sites used for gathering of non-AC data). To put

Table 7
Optimization performance – stochastic vs. deterministic methods.

Antenna		Vivaldi			Monopole		
Optimization method		BO	GA	This work	BO	GA	This work
Site A	E#	–22.38	–22.58	**–23.56** %	–22.49	–23.67	**–23.89** %
	M#	–22.47	–23.14	**–23.66**	–24.81	–25.13	**–25.73**
	$E(\Delta)$$	1.18	0.98	–	1.40	0.22	–
	$M(\Delta)$$	1.19	0.52	–	0.92	0.60	–
Site B	E#	–21.55	**–23.01** %	–22.97	–25.28	–24.63	**–26.60** %
	M*	–22.69	**–23.07**	–22.87	–25.57	–25.26	**–26.45**
	$E(\Delta)$$	1.46	–	0.04	1.32	1.97	–
	$M(\Delta)$$	0.38	–	0.20	0.88	1.19	–

E/M – average/median over all considered frequencies.
$ Performance discrepancy w.r.t. the best results.
% The best results are marked using bold font.

that into perspective, one should emphasize that AC experiments have been performed using the gear tailored to the facility, whereas non-AC data have been gathered using the custom mobile test stands (but also using different cables, active components, and AUT mounting fixtures) (Bekasiewicz et al., 2023; Olencki et al., 2023). Due to the logistic-related reasons, evaluation of the AUT performance in the AC and non-AC conditions with the use of exactly the same gear was not possible.

For the monopole antenna of Section 4.2, the tests conducted in the site A indicate that the correction performance at 7 GHz and 7.5 GHz is not only poor but also consistent across the benchmark methods (cf. Table 3). At the same time, in site B the worsened fidelity of measurements can be observed only at 7.5 GHz. As already mentioned, the discrepancy between the AC and non-AC data can be attributed to the use of different test gear (with particular emphasis on rotary heads and AUT fixtures). Similarly, the frequency-selective misalignment between the results obtained in both sites stem from the use of slightly different gear (i.e., the adapters required for installation of the monopole on the rotary heads). In each site, a different type of custom adapter for AUT—manufactured (additively) from polyethylene terephthalate glycol (PET-G) filament—is used. Due to small size (around 200 mm^2 (Bekasiewicz et al., 2023) omnidirectional radiation properties, as well as low gain, the effects of the used fixture on the far-field properties of the monopole become noticeable (especially at higher frequencies). The reason why the responses obtained in the site B at 7 GHz frequency are much better than the ones from the site A (cf. Tables 3 and 4) is that the experiments performed in the latter one employed a modified adapter that increases flexibility in terms of precise positioning the AUT w.r.t. RA (desired for scanning accuracy). However, it is also characterized by larger dimensions and an asymmetric shape (roughly twice as large compared to the symmetrical adapter used in the site A). The increased dimensions negatively affect the far-field performance of the structure at the mentioned frequencies. Fig. 12 shows a comparison of the antenna radiation patterns obtained from the EM simulations (in setups that account for the adapters, as well as without them) against the AC and non-AC measurements. The responses clearly indicate the negative effects of the asymmetric fixture on the monopole performance. It should be noted, that scaling procedure of (9) exploits the EM simulations without any fixtures which affects (frequency selective) poor correction performance in the site A. The problem concerning accounting for the effects of adapters on far-field measurements accuracy is beyond the scope of this manuscript, and hence will be the subject of future research.

As it comes to the Vivaldi structure of Section 4.1, the discrepancies

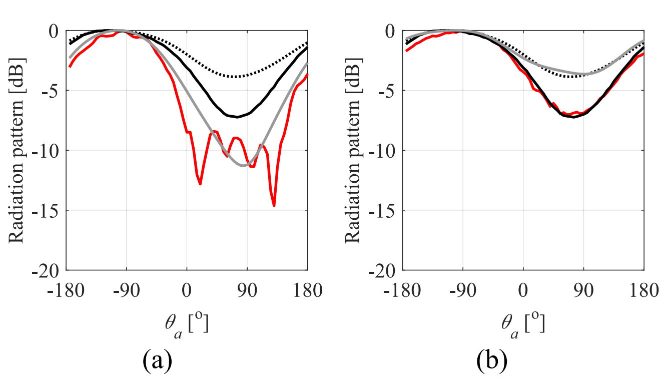

Fig. 12. Comparison of EM simulation responses for the monopole without (⋯) and with (gray) adapters against AC (black) and corrected non-AC (red) measurements at 7 GHz for: (a) site A and (b) site B. In the latter, the EM simulation responses are well-aligned which promotes tuning of post-processing setup. Hence, the AC and non-AC responses are virtually the same. The negative effects of a large fixture used in site A, unaccounted for in the optimization, negatively affect far-field performance resulting in poor correction quality.

between the EM-simulation responses and AC/non-AC measurements shown in Fig. 11 are especially pronounced around the 180° angle of rotation (i.e., in backwards orientation of the AUT w.r.t. RA). The discrepancies at the 180° are exacerbated by the attenuation of (already faint signals) by the adapters used to attach the antennas to the rotary heads. The latter cannot be neglected in the real-world testing scenarios because—in contrary to the monopole of Section 4.1—the feeding port is located behind the antenna (the experiments are performed in yz-plane; cf. Fig. 5(a)), rather than below it (yz-plane; cf. Fig. 5(b)).

5.5. Computational cost of post-processing

The optimization of hyperparameters at each frequency point f_0 involves a few hundred executions of the MPA routine (2), which results in increased computational cost compared to the methods that employ the rule-of-thumb-based tuning. The overall cost of post-processing using the proposed framework corresponds to around 15 min of CPU-time per frequency. The contributing factors include measurements of the RA-AUT transmission in non-AC conditions (estimated to around 4 min on average; the time expenditure associated with setup of the test gear is not included) and optimization of hyperparameters (an average of $\sim$ 11 min on a machine with 8 CPU cores and 32 GB RAM). To put that into perspective, in (Soltane et al., 2020), the average cost of associated measurements in non-AC environment amounts to around 11 min per frequency, which is slightly less compared to the proposed approach. It should be noted, however, that the method of (Soltane et al., 2020) does not involve optimization of the correction setup. Non-negligible cost of the hyperparameters optimization might represent certain limitation of the proposed framework (especially, when rapid correction of *en masse* measurements is required). It is worth noting that the CPU-time associated with pattern search optimization is comparable to the one of GA (around a dozen minutes). This is expected due to a large number of objective function evaluations required by GA. The cost of BO revolved around 3 min of CPU time, yet it also offers the performance that is comparable to standard approaches with manually adjusted setup. Having that in mind, reduction of post-processing cost—albeit beyond the scope of this work—represents an interesting direction for future research.

6. Conclusion

In this paper, a method for automatic determination of hyperparameters to ensure reliable post-processing of non-anechoic measurements has been proposed. The algorithm involves optimization of the matrix-pencil algorithm setup through curve-fitting of the refined non-anechoic measurements to an appropriately scaled EM-based surrogate. Given complexity of the functional landscape and mixed-integer nature of the problem, the optimization is performed using a derivative-free method that undergoes multiple re-sets from a set of initial designs representing the MPA setup. The algorithm has been evaluated based on a total of 400 experiments spanned across two antennas, two test sites, 15 different frequencies of interest, four post-processing routines, and three optimization algorithms. For the considered test sites and antennas, the method offers up to over 14 dB improvement of average responses fidelity w.r.t. the uncorrected non-anechoic measurements. Furthermore, the benchmark against the MPA with rule-of-thumb-based setups indicates that automatic tuning offers up to 9 dB improvement of the correction performance. At the same time, notable changes of the optimized MPA setup as a function of frequency can be noticed. The experimental data demonstrate that the optimization of algorithm parameters might be one of the important considerations for small, low-gain radiators. The second important contributor includes maintaining possibly similar (and small) fixtures for installation of AUT on the measurement gear. It should be emphasized that the proposed algorithm does not rely on engineering insight and thus the post-processing performance is not a subject to bias.

Future work will mostly focus on addressing the challenges associated with utilization of the proposed routine while providing additional insight into the post-processing mechanisms. In particular, a thorough evaluation of the effects of the measurement gear (e.g., mounting fixtures) on the fidelity of the obtained characteristics will be performed. The study will focus on identifying possible gear-induced deterioration of corrected measurement fidelity, as well as development of appropriate mitigation strategies. Another important direction of research involves comparison of the antenna responses obtained in various professional facilities. The availability of such data enables quantitative assessment of the discrepancies between the measured performance characteristics. Furthermore, the mechanisms that could be used to reduce computational cost of post-processing will be investigated. Data-driven machine learning techniques seem to represent a natural choice for development of cost-efficient solutions. Ensuring low-cost response correction while maintaining repeatability and high-fidelity of the results is considered crucial for enabling *en masse* experiments in non-anechoic environments. Finally, the development of methods for automatic tuning of hyperparameters that do not rely on availability of EM simulations will be considered.

Declaration of competing interest

The authors declare that they have no known competing financial interests or personal relationships that could have appeared to influence the work reported in this paper.

Acknowledgements

This work was supported in part by the National Science Center of Poland Grant 2021/43/B/ST7/01856.

Data availability

Data will be made available on request.

References

Araque Quijano, J. L., et al. (2011). Suppression of undesired radiated fields based on equivalent currents reconstruction from measured data. *IEEE Antennas and Wireless Propagation Letters, 10*, 314–317.

Awan, F. G., & Kiran, A. (2017). Cancellation of interference for emission measurement in open area test site. *Measurement, 111*, 183–196.

Bandler, J. W., et al. (2004). Space mapping: The state of the art. *IEEE Trans. Microwave Theory Techn.,, 52*(1), 337–361.

Bekasiewicz, A., Koziel, S., & Czyz, M. (2023). Time-gating method with automatic calibration for accurate measurements of electrically small antenna radiation patterns in non-anechoic environments. Measurement, vol. 208, art no. 112477.

Bekasiewicz, A., & Waladi, V. (2024). Automatic correction of non-anechoic antenna measurements using complex Morlet wavelets. *IEEE Antennas and Wireless Propagation Letters, 23*(8), 2521–2525.

Cano-Facila, F. J., Burgos, S., Martin, F., & Sierra-Castaner, M. (2011). New reflection suppression method in antenna measurement systems based on diagnostic techniques. *IEEE Transactions on Antennas and Propagation, 59*(3), 941–949.

Conn, A., Scheinberg, K., & Vincente, L. N. (2009). *Introduction to derivative-free optimization*. Philadelphia: MPS-SIAM Series on Optimization.

de Sao Jose, A. N., Deniau, V., Resende, U. C., & Adriano, R. (2020). Improving antenna gain estimations in non-ideal test sites with auto-tunable filters. Measurement, vol. 159, art no. 107720.

Dzwonkowski, M., & Bekasiewicz, A. (2024). Auto-correction of non-anechoic antenna measurements based on multi-taper approach. *IEEE Antennas and Wireless Propagation Letters, 23*(11), 3962–3966.

Eiben, A. E., & Smith, J. E. (2015). *Introduction to evolutionary computing*. Springer.

Esmail, B. A. F., Isleifson, D., & Koziel, S. (2024). Dual-band millimetre wave MIMO antenna with reduced mutual coupling based on optimized parasitic structure and ground modification. Science Reports vol. 14, art no. 20507.

Fourestie, B., & Altman, Z. (2001). Gabor schemes for analyzing antenna measurements. *IEEE Transactions on Antennas and Propagation, 49*, 1245–1253.

Froes, S. M., et al. (2019). Antenna radiation pattern measurement in a nonanechoic chamber. *IEEE Antennas and Wireless Propagation Letters, 18*(2), 383–386.

Garnett, R. (2023). *Bayesian optimization*. Cambridge University Press.

Gbadamosi, S. A., Hancke, G. P., & Abu-Mahfouz, A. M. (2024). Adaptive interference avoidance and mode selection scheme for D2D-enabled small cells in 5G-IIoT networks. *IEEE Transactions on Industrial Informatics, 20*(2), 2408–2419.

Gemmer, T. M., & Heberling, D. (2020). Accurate and efficient computation of antenna measurements via spherical wave expansion. *IEEE Transactions on Antennas and Propagation, 68*(12), 8266–8269.

Ghosh, S., Basu, B., Nandi, A., & Das, M. (2024). "Hand activity classification based on perturbed nearfield radiation and augmented impedance of a wearable textile antenna." Expert Systems with Applications, 238, art no. 121830.

Gregson, S. F., et al. (2011). "Application of mathematical absorber reflection suppression to far-field antenna measurements." Loughborough Ant. Prop. Conf., pp. 1-4, Loughborough.

Hemming, L. (2002). *Electromagnetic anechoic chambers: a fundamental design and specification guide*. Piscataway: IEEE Press.

Koziel, S. (2010a). Shape-preserving response prediction for microwave design optimization. *IEEE Transactions on Microwave Theory and Techniques, 58*(11), 2829–2837.

Koziel, S. (2010b). Computationally efficient multi-fidelity multi-grid design optimization of microwave structures. *App. Comp. EM Soc. J.,, 25*(7), 578–586.

Kurokawa, S., Hirose, M., & Komiyama, K. (2009). Measurement and uncertainty analysis of free-space antenna factors of a log-periodic antenna using time-domain techniques. *IEEE Transactions on Instrumentation and Measurement, 58*(4), 1120–1125.

Leon, G., Loredo, S., Zapatero, S., & Las-Heras, F. (2009). Radiation pattern retrieval in non-anechoic chambers using the matrix pencil algorithm. *Prog. EM. Res. Lett.,, 9*, 119–127.

Loredo, S., Pino, M. R., Las-Heras, F., & Sarkar, T. K. (2004). Echo identification and cancellation techniques for antenna measurement in non-anechoic test sites. *IEEE Transactions on Antennas and Propagation, 46*(1), 100–107.

Lyu, Y., Yuan, Z., Zhang, F., Kyosti, P., & Fan, W. (2023). Virtual antenna array for W-band channel sounding: Design, implementation, and experimental validation. *IEEE Journal of Selected Topics in Signal Processing, 17*(4), 729–744.

Olencki, J., Waladi, V., Bekasiewicz, A., & Leifsson, L. (2023). A low-cost system for far-field non-anechoic measurements of antenna performance figures. *IEEE Access, 11*, 39165–39175.

Oppenheim, A. V., & Schafer, R. W. (2009). *Discrete-time signal processing* (3rd ed.). Prentice Hall.

C. Parini, et al., Theory and Practice of Modern Antenna Range Measurements, 2^{nd} ed., vol. 1, IET, Stevenage, 2020.

Rice, A., & Kiourti, A. (2022). High-contrast low-loss antenna: A novel antenna for efficient into-body radiation. *IEEE Transactions on Antennas and Propagation, 70*(11), 10132–10140.

Sarkar, T. K., & Pereira, O. (1995). Using the matrix pencil method to estimate the parameters of a sum of complex exponentials. *IEEE Transactions on Antennas and Propagation, 37*(1), 48–55.

Soltane, A., et al. (2020). Antenna radiation pattern measurement in a reverberating enclosure using the time-gating technique. *IEEE Antennas and Wireless Propagation Letters, 19*(1), 183–187.

Wu, Z., Yu, M., & Liang, J. (2023). "Parameter optimization of energy-efficient antenna system using period-based memetic algorithm." Expert Systems with Applications, vol. 214, art no. 119131.